First-principles modelling of complex perovskite $(Ba_{1-x}Sr_x)(Co_{1-y}Fe_y)O_{3-\delta}$ for solid oxide fuel cell and gas separation membrane applications

Yuri A. Mastrikov,[ab] Maija M. Kuklja,[a] Eugene A. Kotomin*[bc] and Joachim Maier[c]

Received 27th May 2010, Accepted 22nd June 2010
DOI: 10.1039/c0ee00096e

The results of the first principles spin-polarized DFT calculations of the atomic and electronic structure of a complex perovskite $(Ba_{1-x}Sr_x)(Co_{1-y}Fe_y)O_{3-\delta}$ (BSCF) used as a cathode material for solid oxide fuel cells (SOFC) and gas separation membranes are presented and discussed. The formation energies of oxygen vacancies are found to be considerably smaller than in other magnetic perovskites, *e.g.* $(La,Sr)MnO_3$, which explains the experimentally observed strong deviation of this material from stoichiometry. The presence of oxygen vacancies induces a local charge redistribution, associated with the local lattice perturbation, and expansion of the equilibrium volume, in line with the experimental data.

1. Introduction

Development of new environmentally friendly sources of energy nowadays is in a great demand. One promising option are Solid Oxide Fuel Cells (SOFC) with high efficiency of converting chemical energy into electricity. The SOFC performance is to a large degree determined by the catalytic properties of the cathode.[1,2] Most of the mixed ionic-electronic conducting materials traditionally used as SOFC cathodes as well as oxygen permeable ceramic membranes (OPCM) require high operational temperatures, 800–1000 °C. The complex perovskite $(Ba_{1-x}Sr_x)(Co_{1-y}Fe_y)O_{3-\delta}$ (BSCF) material with its unusually large oxygen vacancy concentration and mobility allows for a significant decrease of the operating temperature down to 700–800 °C, retaining its catalytic activity. Understanding properties of this and related materials at the atomistic level may help improve the performance of SOFC and OPCM.

[a]*Materials Science and Engineering Department, University of Maryland, 2135 Chemical & Nuclear Engineering Bldg #090, College Park, MD, 20742-2115, USA. E-mail: yuri@umd.edu; mkukla@nsf.edu; Fax: +(301) 314-2029; Tel: +(301) 405-0221*

[b]*Institute of Solid State Physics, University of Latvia, Kengaraga iela, Riga, LV, 1063, Latvia. E-mail: kotomin@latnet.lv; Fax: +371 713 2 778; Tel: +371 718 7480*

[c]*Max Planck Institute for Solid State Research, Heisenbergstr. 1, D-70569 Stuttgart, Germany. E-mail: e.kotomin@fkf.mpg.de; Fax: +49-711-689-1722; Tel: +49 (0)711 689 1773*

More specifically and speaking in chemical terms, $BaCoO_3$ and similar cobaltates formally require Co to be in the oxidation state of +4 which is hard to realize. There are two ways to stabilize the situation: (i) maintaining the oxygen stoichiometry *via* donation of the electron density from O^{2-} to Co^{4+} what means increase of the chemical bond covalency, (ii) creation of oxygen deficiency *via* charged oxygen vacancies and reduction of Co^{4+} to Co^{3+}.To answer this and other questions, in the present theoretical study we performed modelling of stoichiometric and non-stoichiometric BSCF by means of first principles calculations.

2. Method and computational details

The results were obtained by means of the DFT method as implemented in the computer code VASP 4.6.[3] Inner cores of all atoms were described by ultrasoft pseudopotentials with applied projector-augmented wave method (PAW). The exchange–correlation GGA functional was of PBE-type. It should be noted that more sophisticated GGA + *U* approach was applied recently to oxygen vacancies in simple perovskites.[4] However, use of this approach is hardly possible for our perovskite solid solution by the following reasons: (i) the Hubbard-*U* is commonly used as a free parameter and often fitted to the experimental optical gap, which value in BSCF is small and uncertain; (ii) due to two types of *B*-site cations, we have **two** *U* parameters to be optimized simultaneously; (iii) the magnitude of *U*-parameter depends on

Broader context

Solid oxide fuel cells (SOFC) are promising devices generating energy in an environmentally friendly way, by a direct conversion of fossil and renewable fuels into electricity and high-quality heat. A major challenge in the SOFC improving is to reduce the operating temperature down to 500–600 °C. This needs search of complex perovskites combining high O vacancy concentration (non-stoichiometry) and high vacancy mobility at moderate temperatures, as well as long-term cubic structure stability against transformation and degradation in polluted atmosphere. As we have demonstrated recently [Yu. Mastrikov *et al.*, *J. Phys. Chem. C*, 2010, **114**, 3017], the optimal strategy for developing new SOFC cathode should be based on the combination of key experimental data on oxygen incorporation into material and first-principles thermodynamics/kinetics of oxygen reduction and related processes. In this way, we were able to identify the atomistic mechanisms of key reactions for $(La,Sr)MnO_3$ (LSM) with the emphasis on the rate-determining steps. Based on the present study, we plan to perform similar analysis for BSCF and related complex perovskites.

the ion environment, *e.g.* it was discussed whether the same U could be used in calculations of CeO_2 and Ce_2O_3.[5] This is the more problematic in our case, when Co and Fe ions have quite different surroundings. Amongst potentials supplied with the VASP code, there is a single PAW PBE potential for each of Ba, Sr and Co elements and several potentials for Fe and O, which differ by the number of valence electrons and the basis set cut-off energy, respectively. Our test calculations showed practically no dependence of the lattice constant (<0.05%) as well as the binding energy (<0.4%) of the BSCF on the choice of Fe PAW PBE potentials, thus we have chosen the *standard* Fe ($3d^7 4s^1$) one. For O, we used soft PAW PBE potential, which gives very close to the experimental binding energy and a reasonable bond length for a free O_2 molecule (5.24*e*V and 1.29Å, *cf.* with the experimental values of 5.12*e*V and 1.21Å, respectively).

The $8 \times 8 \times 8$ k-point mesh was created by the Monkhorst–Pack scheme[6] for the ABO_3 unit cell. Atomic charges were calculated by the Bader method as implemented in the Bader computer code.[7] The kinetic energy cut-off for the plane wave basis set is 520*e*V.

3. Defect-free BSCF

First, we calculated lattice constants of four parent perovskites, which represent the BSCF limiting cases with $(x,y) = (0,1)$. These show good agreement with the experimental data (Table 1). Note that Fe shows high spin, whereas Co has intermediate spin, in agreement with previous studies.[4]

According to the experimental data, $(Ba_{1-x}Sr_x)(Co_{1-y}Fe_y)O_{3-\delta}$ demonstrates the best performance for $x = 0.5$ and $y = 0.2$.[1,2,9] *B*-metals, making stronger than *A*-metals bonding with oxygen atoms, have a higher influence on oxygen transport parameters. Thus in our calculations, we fixed $x = 0.5$ and varied y within the range between 0 and 1.

The compound with the composition coefficients $x = 0.5$ and $y = 0.2$ at T = 873–1173 K and $p_{O2} = 0.001$–1atm has a cubic perovskite structure.[10] At low Fe concentrations BSCF is reported to transform into an oxygen vacancy-ordered 2-H type hexagonal perovskite.[11] In order to explore the transformation of properties of the material in cubic perovskite phase for y<0.2, we used the same structure across the whole range of y values. The calculations performed at $y = 0$ are made for the reference purpose only.

Note, that for every composition $x = 0.5$; $0<y<1$ there exist multiple possible structural arrangements. In our calculations we selected only highly symmetrical ones by the following reasons: 1) to avoid an artificial segregation of one type of atoms (clusters, chains, planes) as no segregated regions have been observed or studied experimentally in this material, the more so, experiments indicate **periodic** dopant distribution (superlattice formation) in a similar $(La,Sr)CoO_3$ system,[12] 2) to maximize isotropy (or minimize artificial anisotropy in the material), 3) to make large-scale calculations feasible. Choosing such a supercell model also allowed us to trace a monotonous transition of properties in the whole range of y parameters. We used two supercells in modelling these ordered structures: that with translation vectors of the 5-atom unit cell expanded by $2 \times 2 \times 2$ and $4 \times 4 \times 4$, containing 40 and 320 atoms, respectively. All atoms in the perfect and defective supercells were allowed to relax to the minimum of the total energy. An example of the stoichiometric structure for $x = 0.5$, $y = 0.75$ and $\delta = 0$ is plotted in Fig. 1. Fe cations occupy ¼ of all *B*-sites forming b.c.c. sublattice.

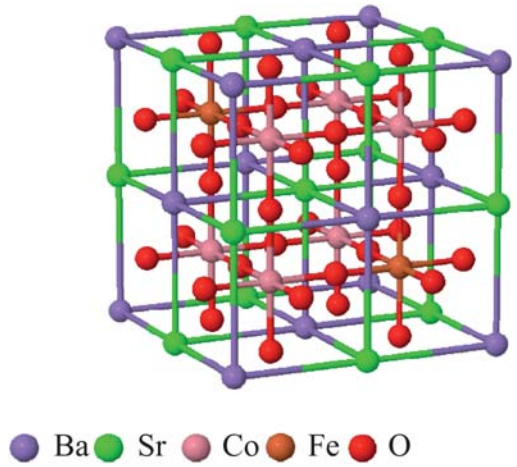

Fig. 1 $(Ba_{0.5}Sr_{0.5})(Co_{0.75}Fe_{0.25})O_3$ $2 \times 2 \times 2$ cubic perovskite 40-atom cell.

Table 1 Calculated lattice constants (in Å) and spins (in brackets) on *B*-atom (in μ_B) for parent ABO_3 cubic perovskites

	B			
A	Co		Fe	
Ba	3.96[a]	(1.96)	3.97[b]	(3.00)
Sr	3.84[c]	(1.89)	3.85[d]	(2.93)

[a] unstable in the cubic perovskite structure; [b] expt. data:[8,9] 4.04Å. [c] expt. data:[8,9] 3.83Å. [d] expt. data:[8,9] 3.85Å.

Cohesive energies calculated on the whole range of y demonstrate a well-defined linear growth from 24.96*e*V for $y = 0$ to 26.23*e*V for $y = 1$. Thus, in BSCF, oxygen forms stronger (by 5%) chemical bonds with Fe ions rather than with Co ions.

A full geometry optimization for stoichiometric ($\delta = 0$) BSCF revealed only tiny ($\leq$ 0.01Å) displacements of oxygen ions surrounding Fe ions for Co- dominated compounds (y<0.5), whereas Fe- dominated compounds (y>0.5) show an undistorted cubic perovskite structure. The optimized lattice constants range in a narrow (3.90–3.92 Å) interval and are smaller by 0.05–0.08 Å than the relevant experimental values for non-stoichiometric (δ>0) BSCF (3.98 Å, $y = 0.2$;[8,9]). In contrast to good agreement with experiment for the parental materials, calculated lattice constants for $x = 0.5$ and y<1 are underestimated, what can be attributed to the neglect of oxygen vacancies in this set of calculations (see below). Note, that at $y = 1$ which corresponds the lowest vacancy concentration in real material, the difference between the experimental and calculated values is less than 1% (3.927[8] *vs.* 3.918 Å, respectively).

The effective atomic (Bader) charges were also calculated and averaged over all ions of the same type (*A* and *B*). Although the absolute charge values depend on the calculation method, they could be used for semi-quantitative understanding of the general trends in the electronic charge redistribution. First of all, the

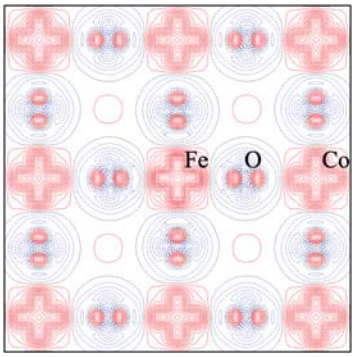

Fig. 2 Difference electronic density map of the $Co_{0.75}Fe_{0.25}O_2$ plane, centred with respect to Fe ion. Solid (red in colour) and dash (blue) lines correspond to positive and negative charge, respectively, with the increment of $0.032e/Å^3$.

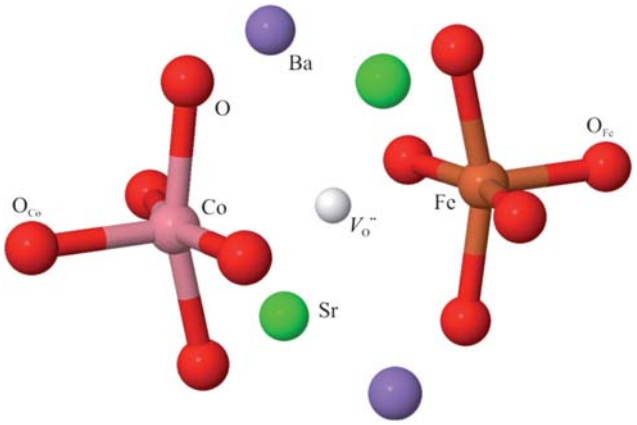

Fig. 3 Sketch of Co-$V_O^{\cdot\cdot}$-Fe type vacancy.

effective charges of both Sr and Ba are close to a formal charge of $+2e$ and practically do not change with composition, whereas the charges on both *B*-metals are much smaller than their formal charges of $+4e$; the effective charge on O is also strongly reduced compared to the formal charge of $-2e$. The latter results from a considerable covalent contribution into the *B*–O chemical bonding, which is typical for ABO_3 perovskites.[13]

As the Co concentration increases, the effective charges of Co ions increase from $1.57e$ reaching the saturation level of $1.61e$ at $y \approx 0.25$. The charge on Fe ($1.66e$ instead of a formal value of $+4e$) demonstrates no dependence on y at all. Since the charge on *B*-ions reaches its minimum value ($q_B = q_{Co}$) at $y = 0$ and the charge on *A*-ions remains constant, the absolute value of the charge on the oxygen is also the lowest ($-1.07e$) at $y = 0$. This may be one of the reasons for the smaller formation energies of oxygen vacancies in Co-rich BSCF (see below). For example, the Bader effective charges in more ionic $LaMnO_3$ are:[14] $-1.29e$ (O), 2.13 (La), $1.85e$ (Mn), to be compared with the formal charges of $-2e$, $+3e$, $+3e$, respectively.

Our previous calculations on $LaMnO_3$ in the ferromagnetic (FM) and three anti-ferromagnetic (AFM) phases- *A*-, *C*- and *G*-AF – have shown[14] that energetic properties are weakly dependent on a particular magnetic order, unless spin polarization is completely neglected.

Thus, we consider here the FM state as the most stable one. The difference electron density map for $(Ba_{0.5}Sr_{0.5})(Co_{0.75}Fe_{0.25})O_3$ (Fig. 2), i.e. the self-consistent electronic density minus the superposition of neutral atom densities, confirms a significant covalent contribution to the chemical bonding between *B*-metals and oxygen.

4. Oxygen vacancy

In order to simulate realistic non-stoichiometric BSCF, oxygen vacancies $V_O^{\cdot\cdot}$ (Fig. 3) were introduced by removing a neutral O atom from the (40- or 320-atom) supercells, which correspond to non-stoichiometries of $\delta = 12.5\%$ and 1.56%, respectively. After O atom removal the electronic density of its two valence electrons (and electrons of other ions) was optimized in the self-consistent procedure, in order to get the minimum of the total energy. Note that we make no *a priori* assumptions on the electron density distribution. The lattice parameters of the cell were fixed as optimized for the ideal structure at $\delta = 0$, whereas all atoms were allowed to relax to the minimum of the total energy.

The oxygen vacancy formation energy in perovskites mostly depends on the distance between the nearest vacancies along the *B*-$V_O^{\cdot\cdot}$-*B* chain (when they are located on the same line along the [100] or symmetrically equivalent direction) or on the distances to the intersection point (*B*-metal) (when two *B*-$V_O^{\cdot\cdot}$-*B* chains lie along the perpendicular directions) rather than on the total concentration of the vacancies. An O vacancy in the 40-atom supercell is repeated along the *B*-$V_O^{\cdot\cdot}$-*B* chain with a period of $2a_0$, that is, the occupied oxygen sites alternate with unoccupied sites along one of four parallel-oriented *B*–O–*B* chains.

The vacancy formation energy was calculated in the standard way, with respect to a free oxygen molecule in the triplet state

$$E_f = [E_{perf} - E_{def} - \tfrac{1}{2} E^{(02)}] \quad (1)$$

where E_{perf} is the total energy of a perfect supercell, E_{def} is the total energy of a fully relaxed supercell with a defect and $E^{(O2)}$ is the total energy of a free oxygen molecule (in the large supercell).

Table 2 Oxygen vacancy formation (frm) and relaxation (lattice polarization, plrz.) energies (in *e*V) in BSCF (with respect to a free O_2 molecule in the triplet state)

		2nd NN B-ion		$\delta = 1/8$		$\delta = 1/64$	
y	vacancy type	Co	Fe	frm.	plrz.	frm.	plrz.
0	Co-$V_O^{\cdot\cdot}$-Co	4	0	1.21	0.98		
0.125	Co-$V_O^{\cdot\cdot}$-Co	4	0	1.21	1.02		
0.125	Co-$V_O^{\cdot\cdot}$-Co	3	1	1.27	1.00		
0.125	Co-$V_O^{\cdot\cdot}$-Fe	4	0	1.39	0.95		
0.25	Co-$V_O^{\cdot\cdot}$-Co	2	2	1.34	1.04	1.04	1.31
0.25	Co-$V_O^{\cdot\cdot}$-Fe	4	0	1.40	0.94	1.12	1.25
0.5	Co-$V_O^{\cdot\cdot}$-Fe	2	2	1.63	1.01		
0.75	Co-$V_O^{\cdot\cdot}$-Fe	0	4	1.92	0.95		
0.75	Fe-$V_O^{\cdot\cdot}$-Fe	2	2	1.82	1.06		
0.875	Co-$V_O^{\cdot\cdot}$-Fe	0	4	2.03	0.98		
0.875	Fe-$V_O^{\cdot\cdot}$-Fe	1	3	2.02	1.01		
0.875	Fe-$V_O^{\cdot\cdot}$-Fe	0	4	2.12	0.98		
1.0	Fe-$V_O^{\cdot\cdot}$-Fe	0	4	2.22	0.96		

In agreement with the calculated cohesive energies mentioned above, the formation energies for vacancies grow with y (Table 2); due to a small difference in the formation energies of Co-$V_O^{\cdot\cdot}$-Co and Co-$V_O^{\cdot\cdot}$-Fe vacancies both vacancy types should exist in almost equal concentrations. The main effect is that increase of Fe content in BSCF considerably increases the vacancy formation energy and thus reduce their equilibrium concentration in the material.

In general, the vacancy formation energy in BSCF being of the order of 1-2eV turns out to be much smaller than those calculated for $LaMnO_3$,[14,15] $E_f = 5.02eV$ or $5.15eV$ in $SrTiO_3$.[13,16] Such small formation energies inevitably lead to high equilibrium vacancy concentrations, orders of a magnitude larger than in $LaMnO_3$, which is a desired property for SOFC cathode materials and oxygen permeable membranes. The calculated trend is also in agreement with experimental estimates that the oxygen vacancy formation energy in $LaCoO_3$ and $LaFeO_3$ ranges from 1.5 to 2eV.[17,18] Note that for a proper comparison charge disproportionation effects (*e.g.* $2Fe^{3+} = Fe^{2+} + Fe^{4+}$) have to be excluded from experimental analysis since these are not taken into account in calculations at 0 K.

Computationally demanding calculations repeated for the large, 320 atom supercell with a very low vacancy concentrations ($\delta = 1.56\%$) show only a small ($\sim$0.2-0.3eV) decrease of the defect formation energy due to reduced interaction between periodically distributed vacancies.

The self-consistent charge redistribution caused by an oxygen atom removal (Table 3) affects mostly the vacancy nearest neighbours – two nearest B-metals and the next sphere neighbour – O ions as shown in Fig.4. This figure demonstrates the total electron density maps (a,b) as well as the two kinds of the difference maps – with respect to the O ion (c,d) and O atom (e,f). These difference maps are plotted as the sum of the self-consistent densities for a defective system plus the density of a missing ion (atom) centered at the vacancy site minus the electronic density of a perfect crystal. Thus, if a vacancy would attract the electron density close to that of a missing ion (the case of ionic oxides like MgO), the difference map with respect to ion shows an excess of the electron density, whereas that with respect to atom negligible difference density. In another extreme case of covalent oxides when a vacancy traps very small electron density the difference density with respect to the ion should be negligible whereas that with respect to the atom shows an excess of the electron density.

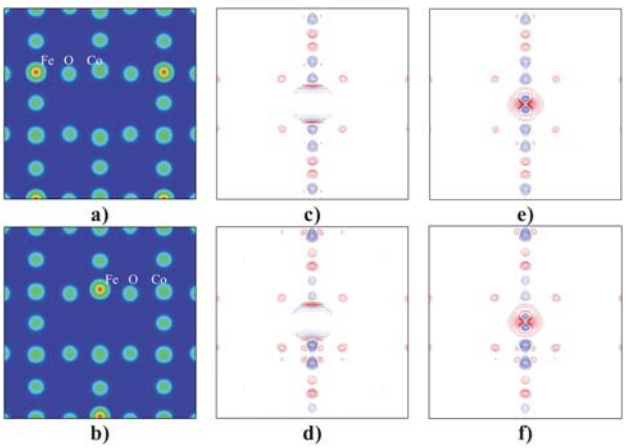

Fig. 4 The total (a,b) and difference (c–f) electron densities in the $(Co_{1.5}Fe_{0.5})O_2$ (001) plane of oxygen vacancy between Co and Co (first row) and Co and Fe ions (second row). with respect to O^- ion (second column) and neutral O atom (right column). Solid (red in colour) and dash (blue in colour) lines in c–f) represent deficiency and excess of the electron density, respectively with the increment of 0.024 e/Å^3.

Table 3 The charge deviations (in e) for ions nearest to the Co-$V_O^{\cdot\cdot}$-Co and Co-$V_O^{\cdot\cdot}$-Fe type vacancies, with respect to the bulk charges at $y = 0.25$. The averaged (over the supercell) deviations of the charges are shown in square brackets with ion symbols in italic; $n\times$ indicate the number of equivalent ions surrounding oxygen vacancy

O O O_{Co}-Co-$V_O^{\cdot\cdot}$-Fe-O_{Fe} O O (Fig.3)				O O O_{Co}-Co-$V_O^{\cdot\cdot}$-Co-O_{Co} O O			3/8 (Fig.5)	
δ atom	1/64	1/8	atom	1/64	1/8	atom	Ba[a]	Sr[a]
2 × Ba			2 × Ba			1 × Ba	−0.11	
[*Ba*]	[-0.001]	[-0.014]	[*Ba*]	[-0.001]	[-0.012]	[*Ba*]	[-0.041]	[-0.038]
2 × Sr			2 × Sr			1 × Sr		−0.06
[*Sr*]	[-0.001]	[-0.007]	[*Sr*]	[-0.001]	[-0.008]	[*Sr*]	[-0.017]	[-0.022]
Co	−0.11	−0.26	2 × Co	−0.11	−0.12	6 × Co	−0.18	−0.18
[*Co*]	[-0.002]	[-0.043]	[*Co*]	[-0.005]	[-0.020]	[*Co*]	[-0.178]	[-0.178]
Fe	−0.11	−0.11	Fe	0.00	0.00	2 × Fe	0.02	0.01
[*Fe*]	[-0.008]	[-0.055]	[*Fe*]	[0.000]	[0.000]	[*Fe*]	[0.016]	[0.013]
8 × O	−0.06	−0.06	8 × O	−0.06	−0.06	18 × O	−0.09	−0.09
O_{Co}	0.00	0.09[b]	O_{Co}[c]	2 × 0.01	0.02	3 × O_{Co}	0.01	0.01
O_{Fe}	0.01	0.09[b]						
[*O*]	[-0.004]	[-0.027]	[*O*]	[-0.004]	[-0.030]	[*O*]	[-0.075]	[-0.075]

[a] three O vacancies form equilateral triangles around Ba and Sr ions (Fig. 6). [b] for $\delta = 1/8$ O_{Co} and O_{Fe} are translationally equivalent. [c] O_{Co} and O_{Co} are symmetrically equivalent for $\delta = 1/64$ and translationally equivalent for $\delta = 1/8$.

As expected, the largest part of the missing oxygen ion charge (-1.07*e*), is attracted by the nearest *B*-metal atoms in the 1st coordination sphere, whereas eight oxygen atoms surrounding vacancy (2nd coordination sphere) receive only ~0.06*e* each. That is, ~0.7*e* is localized on the ions surrounding vacancy. The rest of the charge is distributed among the more distant atoms in smaller (~0.02*e*) portions.

A more detailed analysis shows that nearest Co ions receive larger electron density (0.26*e*) compared to nearest Fe ions (0.11*e*) but an increase of the *averaged* atomic charge is greater for Fe than for Co ions. This is in qualitative agreement with the experimental analysis of the oxidation state variations in non-stoichiometric BSCF based on the XANES spectroscopy and extrapolated to a low temperature region.[19]

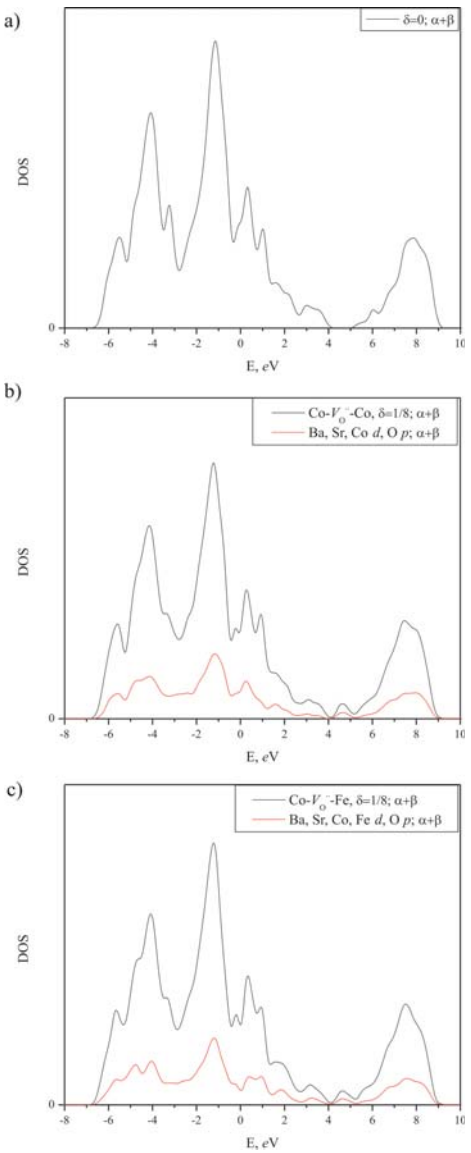

Fig. 5 DOS for the ideal bulk (δ = 0) a), Co-$V_O^{\cdot\cdot}$-Co vacancy b) and Co-$V_O^{\cdot\cdot}$-Fe vacancy at δ = 1/8. Projected DOS is made for the orbitals of the nearest to the oxygen vacancy ions, which give the largest contribution into the peak in the gap. Zero level corresponds to the Fermi energy.

As mentioned above, to illustrate the vacancy-induced spatial charge redistribution qualitatively we plotted in Fig. 4 difference electron density maps with respect to O^- ion and a neutral O atom. The perturbed electron density can be easily attributed to particular ions that are clearly seen on the total density maps (Fig. 4a,b). The purpose of these maps is to give a structural reference for other (Fig. 4c,d,e,f) maps.

A relatively large positive charge density at the vacancy site on the difference electron density maps drawn with respect to a neutral O atom (Fig. 4e,f), indicates that the amount of charge localized directly at the vacancy site is very small (<0.1*e*). This is confirmed by a direct integration of the electron density within the vacancy.

The difference density maps drawn with respect to O *ion*s (Fig. 4c,d) show that the nearest to the vacancy *B*-metal-cations not only gain an additional negative charge, but also are slightly polarized towards the vacancy.

The effect of the electronic structure perturbation caused by oxygen vacancy is illustrated by a comparison of the total and projected densities of states (DOS) for a pure and defective crystal (Fig. 5). As one can see, a vacancy induces additional peaks in the energy range around −0.3 eV and also at 4–5 eV where no states were observed in a pure crystal (*cf.* with the similar study for $SrTiO_3$, Fig. 5 in ref. 16). The main contribution to these additional DOS peaks comes from two *B*-type cations and eight oxygen atoms nearest to the vacancy.

Calculated with respect to the perfect bulk lattice sites, the atomic displacements (Table 4) show the structure perturbation spreading up to the 3rd coordination sphere of the vacancy. Most

Table 4 The largest atomic displacements *d* (in % of a_0) around the oxygen vacancies in the Co-$V_O^{\cdot\cdot}$-Co (a) and Co-$V_O^{\cdot\cdot}$-Fe (b) configurations for 40-atom (**δ** = 1/8) and 320-atom (**δ** = 1/64) supercells at $y = 0.25$, O(Co/Fe) indicates the nearest neighbour(s) of the atom. Positive (negative) sign means outwards (inwards) direction of the displacement

(a)

			d, %	
sphere	atom	N of eq. atoms	δ = 1/64	δ = 1/8
1	Co	2	5.42	2.87
2	O	4	−4.20	−3.73
2	O	4	−2.56	−3.65
2	Sr	2	2.46	2.69
3	O	2	2.86	
6	O	4	−2.62	

[a] Nearest neighbours as for δ = 1/64 except O(Co/Fe) in the 3rd sphere.

(b)

			d, %	
sphere	atom	N of eq. atoms	δ = 1/64	δ = 1/8[a]
1	Co	1	4.54	−0.96
1	Fe	1	5.14	3.11
2	O(Co)	4	−3.55	−3.70
2	O(Fe)	4	−3.67	−3.88
2	Sr	2	2.67	2.84
3	O(Fe)	1	1.63	−1.20
3	O(Co)	1	1.45	

of the cations are shifted outwards from the vacancy whereas oxygen atoms are displaced inwards, due to the electrostatic interactions. The oxygen vacancy also *macroscopically* expands the lattice.

Due to certain anisotropy of the lattice relaxation around a single vacancy, we calculated the change of the supercell volume and recalculated it as a symmetric expansion of the *cubic* supercell. Arranging *three* oxygen vacancies in 40-atom supercell in a particular order (Fig. 6, $\delta = 3/8$) helps to eliminate this effect. These vacancies, lying in non-intersecting and mutually perpendicular *B*–O–*B* chains, form an equilateral triangle either around Ba or Sr ions, what makes expansion of the volume isotropic. For both configurations, the corresponding energies and relaxed lattice constant practically coincide.

The formation energy of oxygen vacancy for the oxygen non-stoichiometry of $\delta = 3/8$ is 1.81 *e*V, considerably larger than for smaller vacancy concentrations discussed above (see also Table 2). The observed increase in the defect formation energy with the degree of non-stoichiometry arises due to increased concentration of reduced Co and Fe atoms in the system.

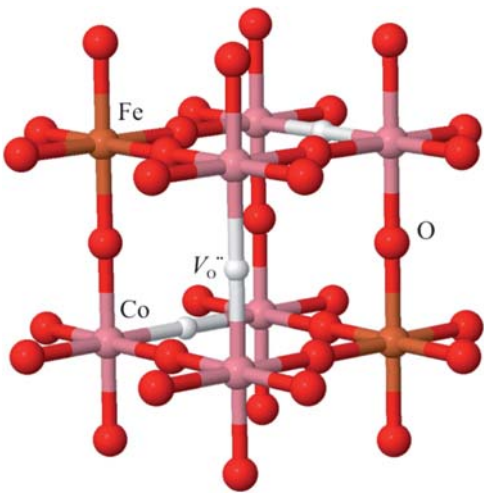

Fig. 6 Ordered oxygen vacancies in $(Ba_{0.5}Sr_{0.5})$ $(Co_{0.8}Fe_{0.2})$ $O_{2.625}$. The Ba/Sr sublattice is not shown for clarity.

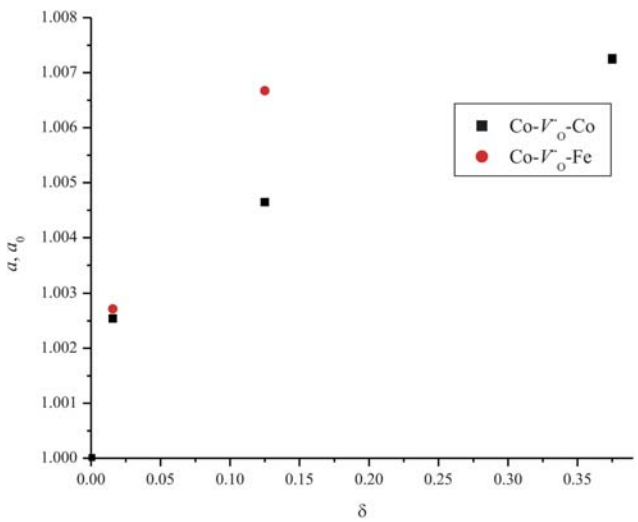

Fig. 7 Relative change of the lattice constant *vs.* oxygen non-stoichiometry.

As shown in Fig. 7, we observe an increase of the cubic lattice constant, linear at low concentrations and nearly saturated at $\delta = 3/8$. This saturation can be attributed to a considerable cancellation of the lattice deformations produced by three closely located vacancies. If one interpolates the obtained trend in the linear region to the typical experimental non-stoichiometries ($\delta = 0.3$), the calculated lattice constant turns out to be in good agreement with the experiments.[8,9]

5. Conclusions

First-principles calculations of the stoichiometric BSCF have shown that the DFT approach combined with large supercells realistically reproduces the atomic structure of the complex perovskite system and their energetics, and therefore can by used for further calculations on, and optimization of similar non-stoichiometric compounds.[20] Due to a considerable contribution of the covalency effects into *B*–O chemical bonding, Co and Fe ion effective charges are much smaller than the formal oxidation state +4. Creation of oxygen vacancy induces additional electronic density on nearest B cations thus reducing their oxidation state.

A detailed analysis of charge redistribution around O vacancy shows that nearest Co ions receive larger electron density fraction (0.26*e*) from a missing O atom compared to nearest Fe ions (0.11*e*) but an increase of the *averaged* atomic charge is greater for Fe than for Co ions. This is in qualitative agreement with the experimental analysis of the oxidation state variations in non-stoichiometric BSCF based on the XANES spectroscopy and extrapolated to a low temperature region.

The oxygen vacancy formation energy in BSCF material is much smaller than for iso-structural $LaMnO_3$ and $SrTiO_3$, in agreement with experiments. This means orders of magnitude increase in vacancy concentrations which is desirable for fast oxygen transport in energy applications.

Further calculations will be focused on defect migration energies in the bulk and on the surface.

Acknowledgements

This work is supported in part by EC FP7 Project NASA-OTM and the US National Science Foundation (NSF) under Grant No. (0832958). MMK is grateful to the Office of the Director of NSF for support under the IRD Program. Authors also thank NSF for its support through TeraGrid resources provided by Texas Advanced Computing Center (TACC) and The National Center for Supercomputing Applications (NCSA) under grant number TG-DMR100021. Any appearance of findings, conclusions, or recommendations, expressed in this material are those of the authors and do not necessarily reflect views of NSF. Fruitful discussions with R. Merkle, A. Roytburd, J. Gavartin, D. Gryaznov, D. Samuelis, V.E. Alexandrov, L. Wang are greatly appreciated.

Notes and references

1 C. Sun, R. Hui and J. Roller, *J. Solid State Electrochem.*, 2010, **14**, 1125.
2 W. Zhou, R. Ran and Z. Shao, *J. Power Sources*, 2009, **192**, 231.
3 G. Kresse and J. Furthmueller, *VASP the Guide. s.l.: Univ. Vienna*, 2003.
4 Y. L. Lee, J. Kleis, J. Rossmeisl and D. Morgan, *Phys. Rev. B: Condens. Matter Mater. Phys.*, 2009, **80**, 224101.
5 G. Jomard, B. Amadon, F. Bottin and M. Torrent, *Phys. Rev. B: Condens. Matter Mater. Phys.*, 2008, **78**, 075125.
6 H. J. Monkhorst and J. D. Pack, *Phys. Rev. B: Solid State*, 1976, **13**, 5188.
7 G. Henkelman, A. Arnaldsson and H. Jónsson, *Comput. Mater. Sci.*, 2006, 254–360.
8 L. Wang, R. Merkle and J. Maier, *ECS Trans*, 2009, **Vol. 25**, 2497.
9 Z. Yang, A. S. Harvey, A. Infortuna and L. J. Gaukler, *J. Appl. Crystallogr.*, 2009, **42**, 153.
10 S. McIntosh, J. F. Vente, W. G. Haije, D. H. A. Blank and H. J. M. Bouwmeester, *Chem. Mater.*, 2006, **18**, 2187–2193.
11 Zh. Chen, R. Ran, W. Zhou, Z. Shao and S. Liu, *Electrochim. Acta*, 2007, **52**, 7343–7351.
12 Z. L. Wang and J. Zhang, *Phys. Rev. B: Condens. Matter*, 1996, **54**, 1153.
13 Yu. Zhukovskii, E. A. Kotomin, R. A. Evarestov and D. E. Ellis, *Int. J. Quantum Chem.*, 2007, **107**, 2956.
14 E. A. Kotomin, Yu. A. Mastrikov, E. Heifets and J. Maier, *Phys. Chem. Chem. Phys.*, 2008, **10**, 4644.
15 Yu. Mastrikov, R. Merkle, E. Heifets, E. A. Kotomin and J. Maier, *J. Phys. Chem. C*, 2010, **114**, 3017.
16 J. Carrasco, F. Illas, N. Lopez, E. A. Kotomin, Yu. F. Zhukovskii, R. A. Evarestov, Yu. A. Mastrikov, S. Piskunov and J. Maier, *Phys. Rev. B: Condens. Matter Mater. Phys.*, 2006, **73**, 064106.
17 J. Mizusaki, M. Yoshihiro, S. Yamauchi and K. Fueki, *J. Solid State Chem.*, 1985, **58**, 257.
18 J. Mizusaki, Y. Mima, S. Yamauchi and K. Fueki, *J. Solid State Chem.*, 1989, **80**, 102.
19 D. Mueller, R. A. De Souza, J. Brendt, D. Samuelis, M. Martin and J. Mater, *J. Mater. Chem.*, 2009, **19**, 1960.
20 J. M. Serra and V. B. Vert, *Chem. Sus. Chem.*, 2009, **2**, 957.